Korean J. Chem. Eng., 37(5), 755-765 (2020)
DOI: 10.1007/s11814-020-0504-7

pISSN: 0256-1115
eISSN: 1975-7220

PIV experimental study on flow structure and dynamics of square stirred tank using modal decomposition

Jie Jin*,,† and Ying Fan***,****

*Shanghai Key Laboratory of Mechanics in Energy Engineering, Shanghai Institute of Applied Mathematics and Mechanics, School of Mechanics and Engineering Science, Shanghai University, Shanghai 200072, China
**School of Energy and Power Engineering, Lanzhou University of Technology, Lanzhou 730050, China
***Department of Process Equipment and Control Engineering, Hebei University of Technology, Tianjin 300130, China
****Research Center of Engineering Fluid and Process Enhancement, Hebei University of Technology, Tianjin 300130, China
(*Received 20 October 2019 • accepted 31 January 2020*)

Abstract−Stirred mixing is one of the important unit operations in the chemical, petroleum, pharmaceutical and food industries. The mixing of liquids is achieved by a rotating shear flow field formed by a periodic jet flow from the impeller. In this work, we investigated the flow structure in a square stirred tank without baffles and with a Rushton impeller (RT) using particle image velocimetry (PIV) technique. The instantaneous flow fields were obtained as a function of various rotations per minute (rpm) for the impeller (N=120, 150, 180, 210 and 240 rpm), while phase-resolved velocity information was obtained for N=150 rpm. The proper orthogonal decomposition (POD) and dynamic mode decomposition (DMD) methods were applied to analyze the velocity fields, flow structure and dynamic information in the absence of impeller area. As demonstrated by the results, there is a wide range of spatial and temporal scales throughout the process. The high energy parts exist in two kinds of structures except for the average fluid flow. The instability phenomenon results from the cyclic shear flow and the trailing vortices structure caused by the periodic jet near the blade passage frequency. As the Reynolds number is on the rise, the periodic flow increases, the random turbulence is reduced, and the flow tends to the ultimate stable state. The square section acts like baffles to change the direction of the fluid circumferential velocity while increasing the radial and tangential flow, which is conducive to mixing. This study provides a basis for understanding the flow structure and unsteady characteristics in a square stirred mixing tank.

Kerwoeds: Flow Characteristic, Square Stirred Tank, PIV, POD, DMD

INTRODUCTION

Flow experimentation is an important method for investigating flow characteristics and has been widely conducted by applying different techniques. The PIV technique plays an important role in flow measurement with high spatial and temporal resolution. This advanced technology has been widely applied in the relevant research [1-4]. However, due to the unsteady characteristics of turbulence and the interaction between different mechanisms, these experimental results are neither directly used nor easily interpreted in many cases. There is a need for feature information to be extracted from a substantial amount of data. The modal decomposition method based on feature extraction technology represents an effective method to analyze the temporal and spatial correlation characteristics of turbulence. The proper orthogonal decomposition (POD) and dynamic modal decomposition (DMD) are considered as the two most significant methods.

POD technology provides an approach to obtaining a series of optimal orthogonals by performing eigen decomposition from a large amount of experimental or numerical data in the meaning of least squares [5,6]. In the study of turbulent velocity field, POD decomposition can be used to identify the structures of various levels by linking the energy and coherent structures involved. POD analysis is extensively involved in turbulence research [7].

DMD technology is one of the latest post-processing tools. This method approximates the flow evolution as a linear dynamic process. The major characteristics shown by unsteady flow can be extracted by eigen decomposition of an experimental data or numerical simulation results [8-10]. It provides assistance in obtaining spatial modes and time coefficients with a single frequency and growth rate and removes the need to establish any additional control equations [11,12]. As for complex flow, it requires comparative analysis to be conducted using POD and DMD methods [13-15].

The working process in a stirred reactor is a complex turbulent flow with unsteady and multi-scale characteristics. Turbulence generation is determined by the stirring system. In general, the characteristic structure is closely related to blade diameter. A large-scale structure is dissipated into heat by viscous force as a result of complex cascades effect. For better understanding of the physical mechanisms in relation to these flow structures and their spatial-temporal characteristics, some studies have been conducted using the POD method to conduct quantitative analysis of the hydrodynamic characteristics exhibited by stirred reactors [16-20].

A square stirred tank shows such advantages as high reaction efficiency, easy manufacture and capability of industrial enlargement [21,22]. In spite of this, there remain few studies focusing on the flow

†To whom correspondence should be addressed.
E-mail: jinjie01@sina.com
Copyright by The Korean Institute of Chemical Engineers.

characteristics of square stirred tank. In the past, more attention has been paid to the wake structure and the local flow characteristics. The mixing and chemical reaction processes take place in the whole stirred tank. Modal analysis is very effective if more comprehensive flow information is required. There is still no report on the POD and DMD analysis of the flow characteristics shown by a square stirred tank. Therefore, the focus of this study was placed on the turbulence characteristics in a square stirred tank, which is in a nearly complete flow area. The POD and DMD methods were applied to the instantaneous velocity field for comparison with the phase-resolved velocity field.

The paper is organized as follows. In Section 2, the experimental setup and procedure are outlined. In Section 3, we use three methods to analyze and discuss the experimental results. Finally, there are several conclusions and perspectives.

EXPERIMENTAL SETUP AND PROCEDURE

1. Experimental System

The stirred-tank configuration under investigation and the general arrangement of the test system are illustrated in Fig. 1 and Fig. 2, respectively. The tank is made of transparent acrylic with flat bottom and square cross section. The Rushton impeller, consisting of six straight blades, has a diameter of D=T/2=80 mm and is located C=T/3=66.7 mm from the tank bottom. The tank diameter is T=160 mm, the liquid height is H=T5/4=200 mm, and the liquid is about 5.12 L (density ρ_L=998 kg/m^3, kinematic viscosity ν_L=1.002×10^6 m^2·s^{-1}). The system is powered by a servo motor, with the speed error restricted to within 1 r/min. A high precision encoder is fitted on the shaft. The phase-resolved photography is performed using the feedback signal of encoder to trigger the PTU.

In this experiment, the Lavison test system with one camera was employed. The camera is Image MX4M with a resolution of 2,048× 2,048. The laser is LPY700 with 100 Hz and 100 mJ as supplied by Litron company. In the process, it applies 2D-2C test method. The test plane passes through the axis while being perpendicular to the lateral wall of the stirred-tank. To reduce the reflection effect produced by free interface and solid wall, the impeller is coated in black, and the PLIF technique is applied. The tracer particles are PS fluorescent particles, and the fluorescent agent is rhodamine B. The Particle size ranges roughly from 20 to 50 μm with a density of 1.05 g/cm^3. The wavelength of laser emission is 532 nm, the excitation wavelength of the fluorescent particle is 612 nm, and the laser thickness is set to 1 mm. The camera was loaded with 540 nm cut-off filter to prevent the reflection of light.

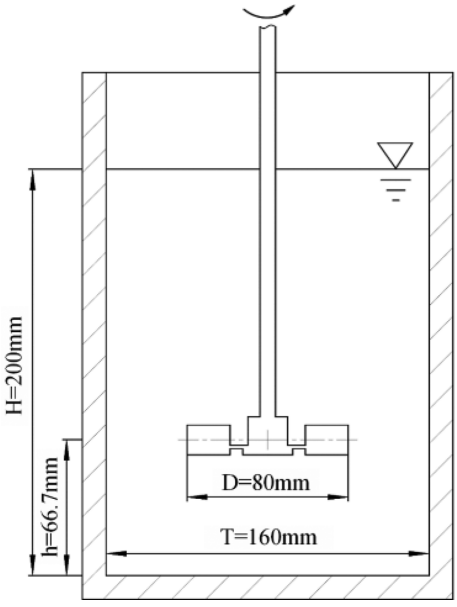


Fig. 1. Front view of stirred device.

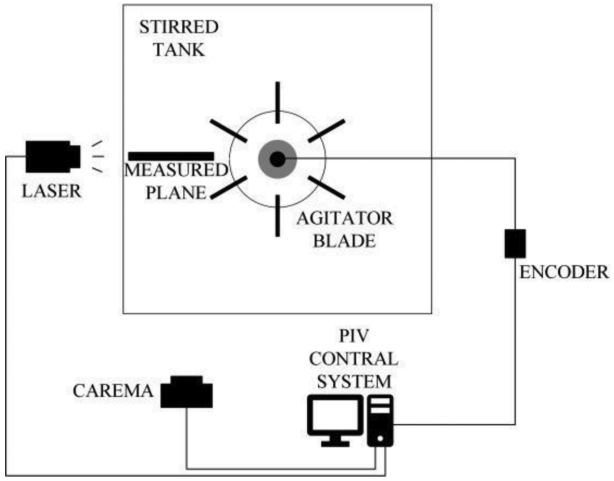


Fig. 2. General arrangement of test system.

The rotational speed N of the Rushton impeller ranges from 150 to 200 rpm with high efficiency. The data is captured by phase-locked photography at a sampling frequency of 2.5 Hz. The sampling phase interval is set to 10°, and 500 pairs of data are collected at each phase angle. The instantaneous velocity fields are measured for 120, 150, 180, 210 and 240 rpm, respectively. The Reynolds number is 1.3× 10^4, 1.6×10^4, 1.9×10^4, 2.2×10^4 and 2.5×10^4, respectively. For each rotational speed, totally 3000 pairs of data are collected at a sampling frequency of 50 Hz, which complies with the requirement of Nyquist sampling theorem. The data calculation query window is 32×32 pixels, and the physical distance is 0.95 mm. In this study, the focus was not placed on dissipative scale, but the size of query window was fully compliant with the requirements of Taylor micro scale structure calculation and analysis [23].

During the experiment, the image of PIV is supposed not to be subject to deformation, the image magnification is a constant, and the error is usually estimated to be roughly 0.3% [24]. For the time separation, the high-speed camera used in the experiment shows an accuracy of 0.05% [25]. The pixel resolution is determined by a number of sources including the particle image diameter, peak locking, velocity gradient, and so on [26]. For the present configuration, the error in measuring particle displacement is estimated at about 2.5% of the measured values. Therefore, the overall uncertainty in the present velocity measurements is estimated to be less than 3%.

2. Data Processing Methods

The post-processing methods applied in this study were POD

and DMD methods based on feature extraction. The feature extraction method is purposed to identify a set of low-dimensional subspaces, and to represent high-dimensional and complex unsteady systems as the superposition of these subspaces in low-dimensional coordinate systems. The spatial-temporal evolution of the corresponding system is described in low-dimensional space. The mathematical expression is shown as Eq. (1) below:

$$\psi_t = \sum_{i=1}^{n} \theta_i(t)\phi_i(x) \tag{1}$$

There is a necessity to establish spatial-temporal correlation matrix prior to post-processing. First, the data at each time are assigned into a corresponding column vector. For scalar, it is arranged in order directly. For vector, one component is arranged in the first place, while the other is arranged after completion. The column vectors of the first N moments are arranged in rows to establish a spatial-temporal correlation matrix:

$$U = [u_1, u_2, u_3 \cdots u_n] \tag{2}$$

The significant difference between POD and DMD methods is that the feature extraction criteria differ. The two methods are described as follows.

2-1. Proper Orthogonal Decomposition

The POD technique is applied to decompose the flow field into multiple spatial orthogonal modes based on the energy of each mode, for which the main modes are selected to identify the coherent structure in turbulence. The relevant mathematical deduction process can be referred to in Sirovich [6] and Lumley [27]. Below is a simplified calculation process of the snapshot POD algorithm applied in this study. Over the course of calculation, the signal is decomposed by scale, and the proper basis functions are identified in a set of basis functions which satisfy the following formula:

$$\langle (u, \phi)^2 \rangle / (\phi, \phi) = \lambda \tag{3}$$

This projection maximization basis function is required to meet the Fredholm equation:

$$\int R(x, x')\phi(x')dx' = \lambda\phi(x) \tag{4}$$

As for the snapshot method, the covariance matrix of the first n snapshots can be established by:

$$R = \frac{1}{n}(U^T U) \tag{5}$$

The covariance matrix is decomposed into eigenvalues, based on which formula 6 is obtained:

$$R\phi = \lambda\phi \tag{6}$$

The POD modes are derived from normalizing the basis functions satisfying the above-mentioned properties with their own L2-norms. The time coefficient can be calculated by applying Eq. (7) as:

$$\theta(t) = (\phi^{pod})^T U \tag{7}$$

The main field modes can be extracted according to the eigenvalues, by ordering the modes based on the energy. By applying Eq. (1), field information can be obtained regardless of time, and the accuracy of reconstruction is determined by the number of modal orders. In the process of deformation, the SVD can also be applied to spatiotemporal correlation matrix, and it may have better robustness.

2-2. Dynamic Mode Decomposition

As a linear, infinite-dimensional operator, the Koopman operator can describe the evolution process of observations for any linear or even non-linear dynamic system. Premised on the Arnoldi algorithm [28] to calculate the DMD modes, the DMD algorithm approximates the observed value of the Koopman mode. DMD analysis can be treated as a numerical approximation of Koopman spectrum analysis. When the number of snapshots increases to a certain level, DMD method is made suitable for non-linear systems. The purpose of DMD technology is to extract dynamic information, and to identify spatial structures at a specific frequency as well as their time coefficients. A brief description of the calculation process is made as follows.

First, two spatial-temporal correlation matrices are constructed below:

$$U_1^{n-1} = [u_1, u_2, u_3 \cdots u_{n-1}] \tag{8}$$

$$U_2^{n} = [u_2, u_3, u_4 \cdots u_n] \tag{9}$$

Due to the same time interval distribution, the flow sequence can be represented by Krylov ordinal number:

$$U_2^n = A[u_1, A^1 u_2, A^2 u_3 \cdots A^{n-2} u_{n-1}] \tag{10}$$

When the number of snapshots n reaches the critical value, the n-th vector can be linearly represented by the first $n-1$ vector:

$$u_n = U_1^{n-1} a + r \tag{11}$$

$$a = [a_1, a_2, a_3 \cdots a_{n-1}]^T \tag{12}$$

$$U_2^n = AU_1^{n-1} = U_1^{n-1} S + re_{n-1}^T \tag{13}$$

In the expression, r indicates the residual vector and e denotes the unit matrix. Matrix A refers to a coefficient matrix describing the dynamic mechanism of system evolution, which shows high dimensions and is unknown. Therefore, the adjoint matrix S of A is taken as the low-dimensional approximation of A in the DMD method. The expression of S is shown as follows:

$$S = \begin{bmatrix} 0 & & & & a_1 \\ 1 & 0 & & & a_2 \\ & 1 & 0 & & a_3 \\ & & \ddots & \ddots & \vdots \\ & & & 1 & a_{n-1} \end{bmatrix} \tag{14}$$

However, when calculating S, the matrix is frequently ill-conditioned, especially when the snapshot data is polluted by noise or other factors. To resolve the above-mentioned problems, the full rank matrix with a greater robustness [29] can be constructed by Vandermonde matrix, QR decomposition or SVD [9]. With regard to full rank matrix eigenvalue decomposition, the basis function and eigenvalue are obtained. The real part and the imaginary part of the eigenvalue represent the growth rate and frequency characteristics of the observed values, while the time coefficient can be

calculated by Gram matrix. The specific calculation formulas are as follows:

$$S\phi = \lambda\phi \tag{15}$$

$$\phi^{DMD} = U_1^{n-1}\phi \tag{16}$$

$$f = \ln|\lambda|/\Delta t \tag{17}$$

$$g = \arg(\lambda)/\Delta t \tag{18}$$

$$\theta(t) = (\phi^{DMD*}\phi^{DMD})^{-1}\phi^{DMD*}U_1^{n-1} \tag{19}$$

RESULTS AND DISCUSSION

1. Phase-resolved Velocity Field

In this study, a six bladed structure Rushton impeller is used, each blade passage angle of which is 60° and the measured plane interval angle of which is 10°. The phase-resolved velocity field is obtained from the data average calculation of each plane, dimensionless calculation of velocity πND (N=2.5 rps), and the diameter of tank T, with the results presented in Fig. 3. They are dimensionless velocity fields of six angles φ ranging from 0-50°, respectively. As revealed by these velocity fields, the flow structure of the Rushton propeller is a typical periodic jet, and the liquid is discharged from the radial direction. Due to the effect of the tank wall, when the fluids contact the wall, they flow to both the upper and lower sides, which contributes to two large circulation loops in the container. There are two wake vortices distributed on both sides of the jet, with the jet direction being slightly upward, thus forming a certain jet inclination angle with the horizontal direction [2]. The angle of jet is different than the non-baffled circular section reactor. The square section acts like baffles, which change the direction of the fluid circumferential velocity while enhancing the radial and tangential flow, which is conducive to mixing [30].

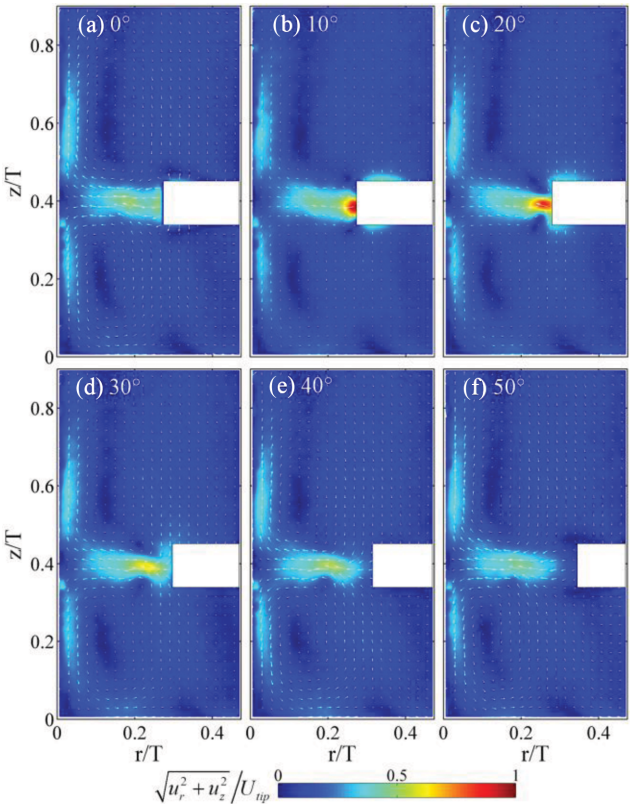


Fig. 3. Phase-resolved velocity fields at different phase planes: (a) φ=0°; (b) φ=10°; (c) φ=20°; (d) φ=30°; (e) φ=40°; (f) φ=50°.

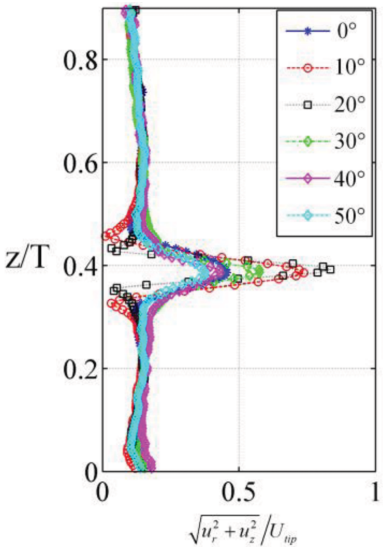


Fig. 4. Impeller outlet velocity profile at different phase planes.

The outlet velocity profiles at different phase angles are illustrated in Fig. 4. When the blade rotates before the 0° plane, the fluid starts to accelerate. Local low values exist at 10° and 20° due to the wake structure, while the peak velocity is observed near the phase angle of 20°. The maximum velocity of the fluids discharged from the radial direction of the impeller is roughly 0.8 times the dimensionless velocity. There is a large velocity gradient near this phase angle. As the phase angle increases, the velocity declines gradually. When the phase angle approaches 60°, the rear blade starts to accelerate the fluid movement and the velocity increases, before entry into the next passage of the blade.

λ_{ci} is a vortex detection method by velocity gradient tensor [31]. When the velocity gradient tensor contains a pair of conjugate complex eigenvalues, there is a vortex structure in the local flow field. Not only can the λ_{ci} criterion distinguish the region of vorticity motion, but also reflect the intensity of vorticity motion. However, it is incapable of indicating the direction of rotation, which makes the direction of vorticity usable. The distribution of λ_{ci} is illustrated in Fig. 5. There are two local high value regions discovered in front of the blade outlet in the 0° plane, which is the wake structure of the last blade passage that incompletely dissipated. The local wake structure can be observed in the 10° plane. On the 20° phase plane, the structure of the vortex and the position of the vortex core can be clearly distinguished, and the intensity of the vortices reaches its peak before decline. By comparing the velocity distributions of different sections, it is found that the position of the vortex core moves outward and the intensity of the vortex decreases as the rotation angle increases. The wake structure does not completely dissipate in a blade passage, which is generated in the blade passage ranging from 0° to 80°.

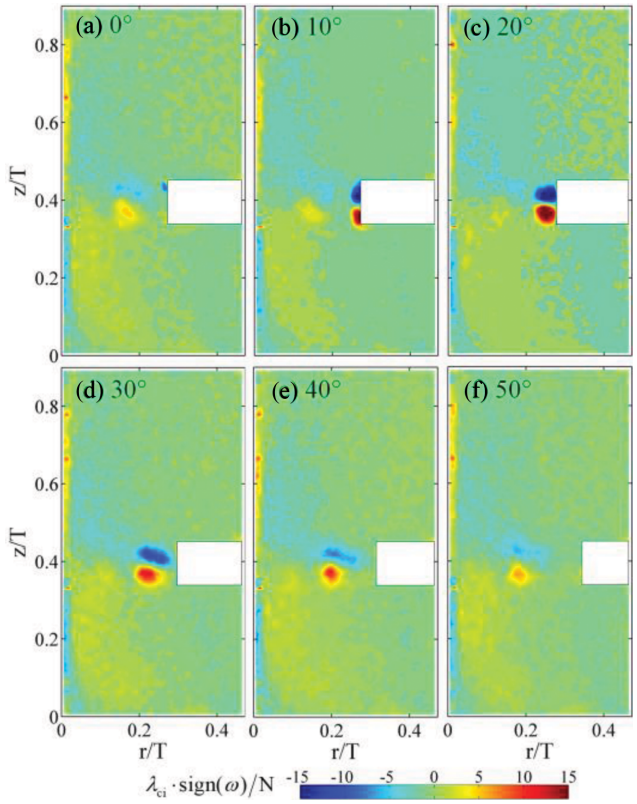


Fig. 5. Phase-resolved distribution of λ_{ci} at different phase planes: (a) φ=0°, (b) φ=10°, (c) φ=20°, (d) φ=30°, (e) φ=40°, (f) φ=50°.

The phase-resolved velocity field is capable of capturing the flow structure at a specific frequency; for example, the wake structures generated by the periodic jet, which results from the same frequency as the blade passage. With regard to other frequency structures, there is a possibility for significant errors to occur. Modal analysis method is more effective if more flow information is required.

2. Analysis of POD

The velocity signal is decomposed using the POD method. The

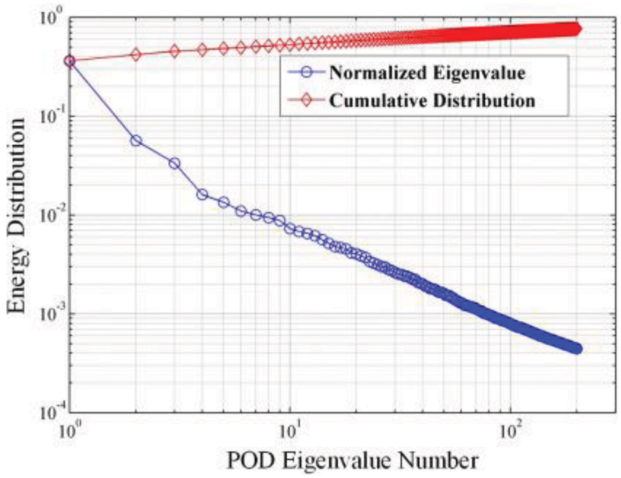


Fig. 6. POD modal energy distribution (N=2.5 s^{-1}).

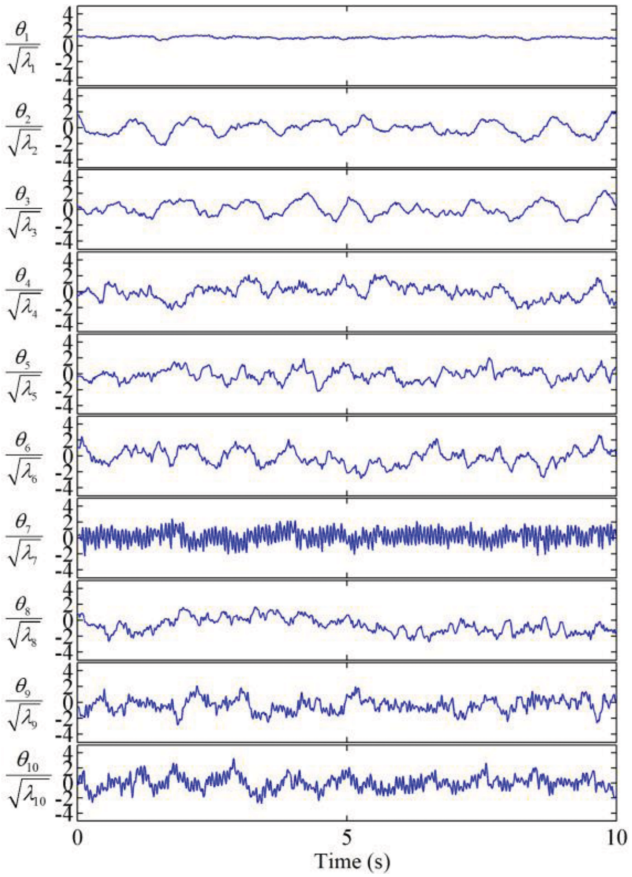


Fig. 7. The POD Time coefficient distribution (modes 1-10).

eigenvalues obtained by POD decomposition correspond to the contribution made by each mode to the total energy in the measurement plane. Fig. 6 presents the energy distribution of the first 200 modes. The energy content of the first order mode is approximately 36%, which represents the average flow and accounts for the highest proportion of energy. Nevertheless, the energy content of first-order modes is lower, indicating that the energy content of velocity fluctuation is higher. Besides, there is a larger arrangement of spatial and temporal scales in flow structure. As shown in Fig. 7, the first-order modal time coefficient is close to a constant, with the rest being wave structures. Based on the principle of POD optimization, it is unlikely to separate the flow based on frequency. In general, the modes consist of multiple frequencies flow structures, and the time coefficients are in the superposition of different frequencies.

The time coefficient is calculated by FFT. The distribution of power spectral density (PSD) for the first ten modes is shown in Fig. 8. The peak value of the first order mode is 0 Hz, which also indicates that the mode corresponds to the average flow. The second to the sixth modes are of large-scale structures with low frequencies. The peak value of the second to third order modes is approximately 0.8 Hz, and the peak value of the fourth to seventh order modes ranges from 0 to 1 Hz, which conforms to correlative flow structures. It is different from the phenomenon of precession vortices macro instability [32,33]. The peak values of the eighth to

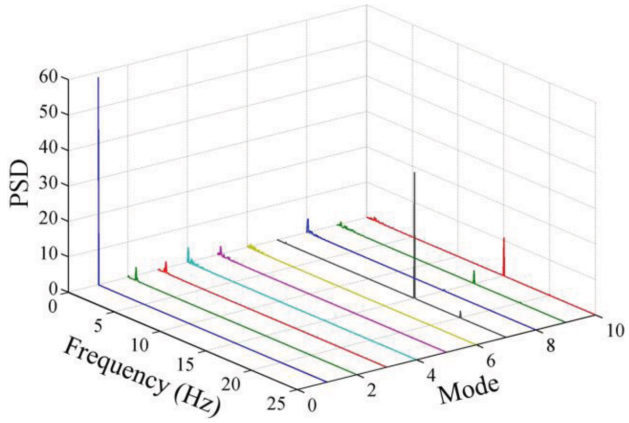


Fig. 8. Power spectral density distribution.

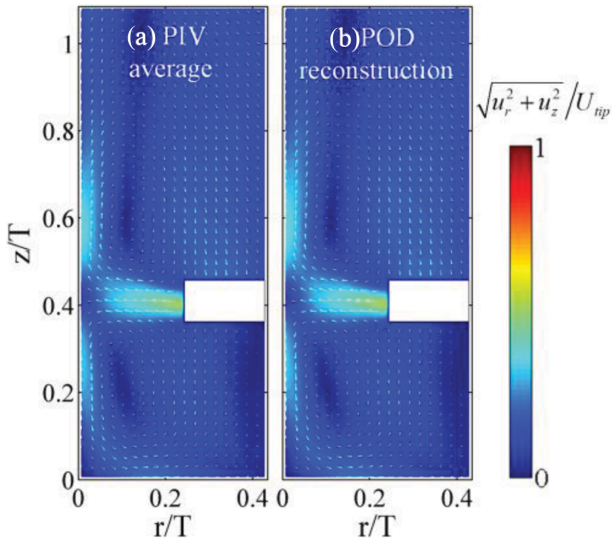


Fig. 9. POD reconstruction velocity field: (a) PIV average velocity field, (b) reconstructed velocity field by POD.

tenth order modes are invariably distributed around 15 Hz, which is consistent with the blade passage frequency. The results demonstrate that the instability flow and the periodic jet generated by the impeller rotation conform to the high energy structures during the blade operation with the exception of the average flow.

Fig. 9 shows a comparison of the velocity field reconstructed by the first order mode with the PIV mean flow field, which exhibits an excellent consistency [18]. The second to sixth order spatial modal structure is illustrated in Fig. 10(a)-(e). It is primarily a large-scale vortex structure generated by cyclic shear flow in the stirring process. One of the causes is the adoption of a relatively large diameter ratio. The seventh and tenth order spatial modes are shown in Fig. 10(f) and (i), which reveals the flow structure generated by

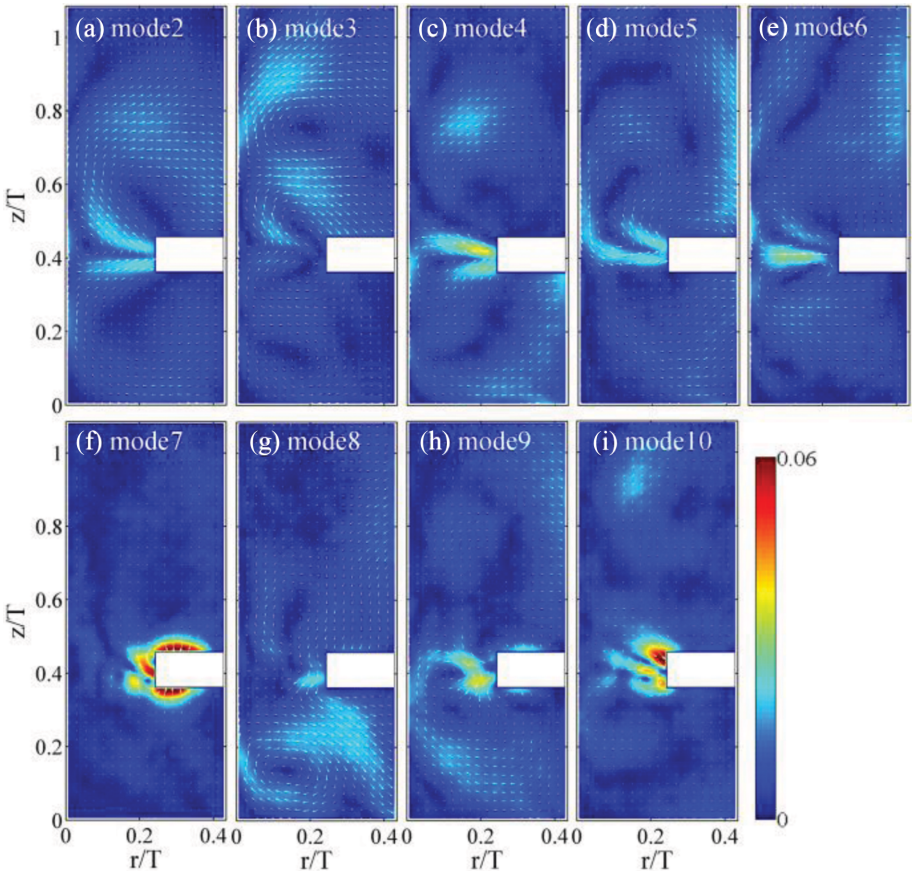


Fig. 10. POD spatial modes distribution: (a) mode2, (b) mode3, (c) mode4, (d) mode5, (e) mode6, (f) mode7, (g) mode8, (h) mode9, (i) mode10.

the strong shear of periodic jet. This is consistent with the analytical results of time coefficient and power spectral density. The spatial distribution law shows similarity to the result of phase-resolved velocity field. The POD method is applied to conduct analysis of periodic flow; the low order modes perform well in the extraction of large-scale coherent structures, while the high order modes fail to show specific coherent structures, exhibiting random motions.

The PSD analysis is conducted of the POD time coefficients at five different rotational speeds. The distribution law is basically identical. The local high value areas are the frequency of blade passage and the low frequency area of instability structure, which suggests that the flow structure is highly similar at different rotational speeds.

Fig. 11 presents the POD energy distribution at five rotational speeds and reveals that the overall distribution is consistent. As the Reynolds number is on the rise, the average flow energy increases. Compared with 120 rpm, the average flow energy increases by roughly 6% at 240 rpm, and the random turbulence is weaker. For the stirring process, an excessively high rotational speed will cause an increase in the energy content of large-scale coherent structure and the solidification of flow structure, as a result of which the reaction speed will not necessarily decrease with the increase of rotational speed.

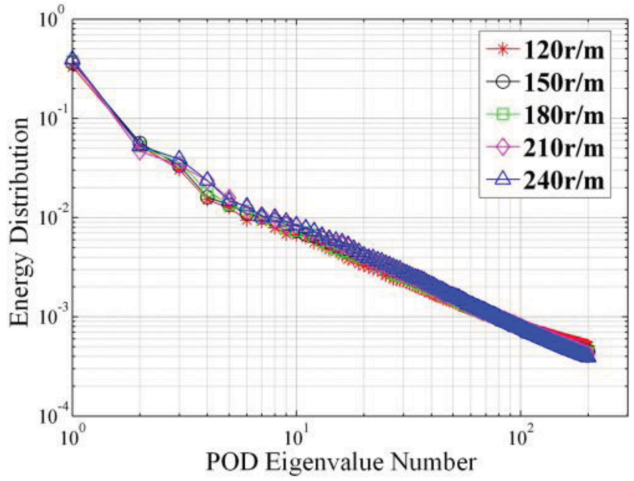


Fig. 11. POD energy distribution at different speeds.

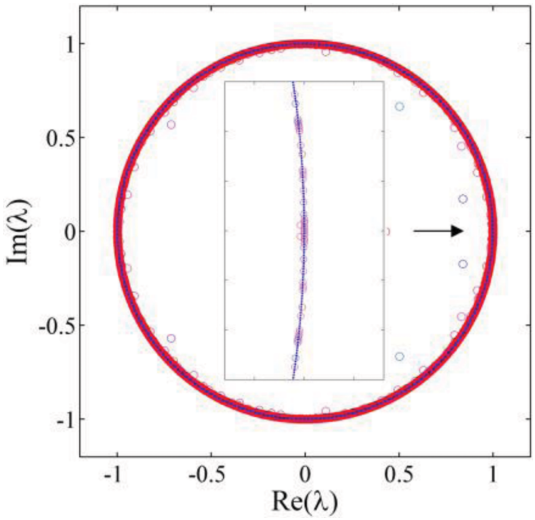


Fig. 12. All DMD eigenvalues distribution.

3. Analysis of DMD

The same velocity signal is analyzed using the DMD method. Eigenvalues are shown in Fig. 12, where the black dotted line indicates a unit circle, representing the steady flow structure. The point in the unit circle represents the dynamic attenuation structure, the point outside the unit circle represents the dynamic growth structure. Most of the eigenvalues are located near the unit circle, and a small number of points are located in the unit circle. In this case, the system is in an unsteady equilibrium state and shows insufficient developed turbulence. Fig. 13 shows how the growth rate is distributed. At the obtained frequencies, the distribution of growth rates is concentrated within the range between −0.5 and 0, with a certain attenuation shown. A small proportion of them are distributed between 0 and 0.1, which conforms to growth structures. The overall distribution law of growth rate exhibits consistency with the result of eigenvalue distribution.

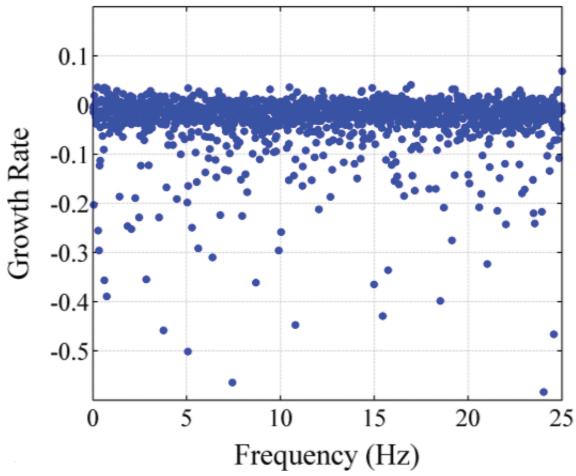


Fig. 13. Growth Rate distribution.

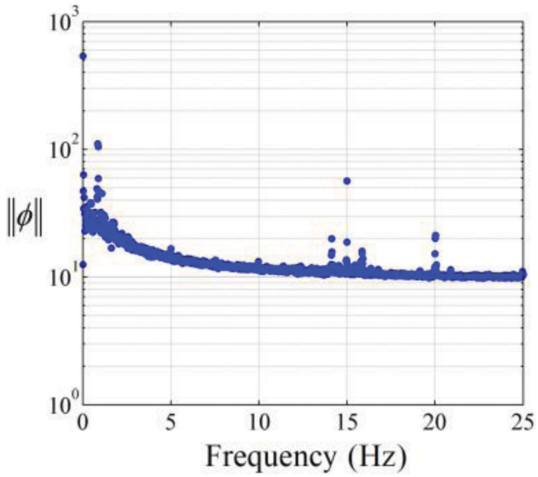


Fig. 14. Amplitude distribution of 2-Norms.

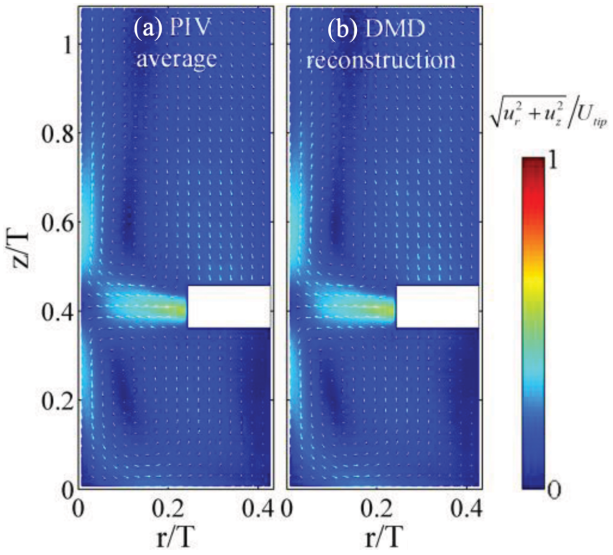


Fig. 15. Velocity field reconstruction by DMD: (a) PIV average velocity field, (b) reconstructed velocity field by POD.

The criterion of modal selection is primarily determined by the 2-norm amplitude of the corresponding modal. The ordinate axis represents the distribution of the amplitude. As the frequency can be expressed as the imaginary part of the eigenvalue divided by 2π, the horizontal ordinate indicates the distribution of the frequency in the corresponding mode. Eigenvalues are shown in the form of complex conjugation, with only modal distributions with non-negative frequencies presented in Fig. 14. By ranking all modes in line with the magnitude criterion, it is obvious that the corresponding magnitudes close to 0.8 Hz and 15 Hz are noticeably higher compared to the other modes except for the average flow.

The first mode of DMD is the real part mode, while the others are the complex modes. The reconstructed model conforms well to the average flow field obtained by PIV test, as shown in Fig. 15. Though the spatial distribution of modes is associated with the real part, only the real part is presented here. Fig. 16 indicates the second to sixth order modes as obtained using the DMD method. The second to fifth order modes are unstable structures generated by cyclic shear flow. The sixth order mode performs excellently in capturing the wake structure generated by periodic jet in blade passage. Moreover, it is consistent with not only the POD method but also the results of phase-resolved method. The DMD method can be effective in extracting large-scale coherent structures for periodic flow and quasi-periodic flow.

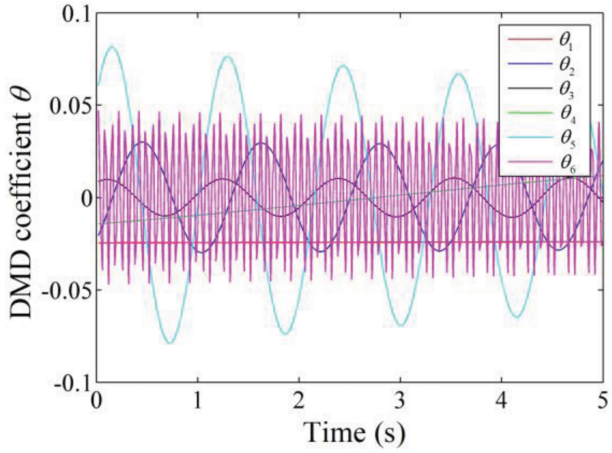


Fig. 17. DMD time coefficients distribution of the first 6 modes.

Fig. 17 illustrates the distribution of time coefficients for the first six modes of the DMD method. The real part coefficient of the first mode shows no periodical change, and the imaginary part coefficient equals zero. The time coefficients of other modes are more complex, thus showing a traveling wave structure with single wave pattern, which makes them different from the time coefficients of POD method [15]. The PSD distribution of the first five modes is determined by the power spectral density analysis of time coefficients, as shown in Fig. 18. As anticipated, the mode shows a single frequency. The peak value of the first order mode corresponds to 0 Hz, while the flow structure corresponds to the average flow.

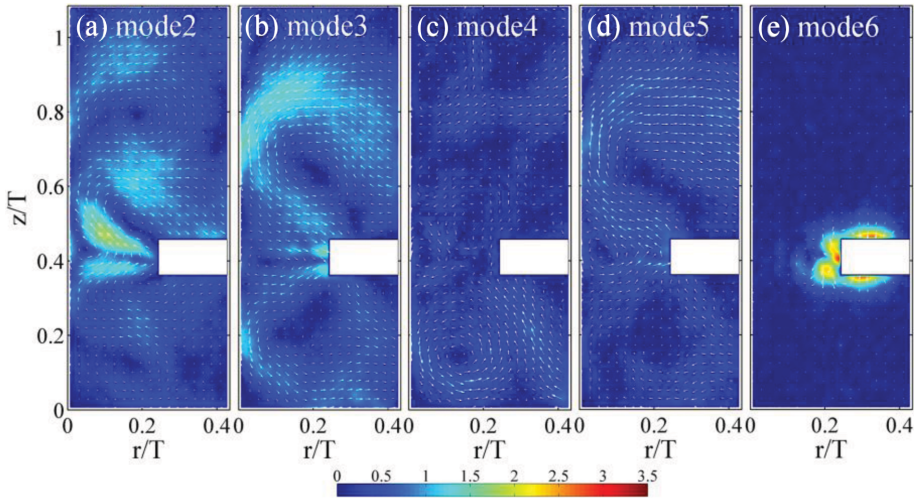


Fig. 16. DMD spatial modes (2-6) distribution: (a) Mode2, (b) mode3, (c) mode4, (d) mode5, (e) mode6.

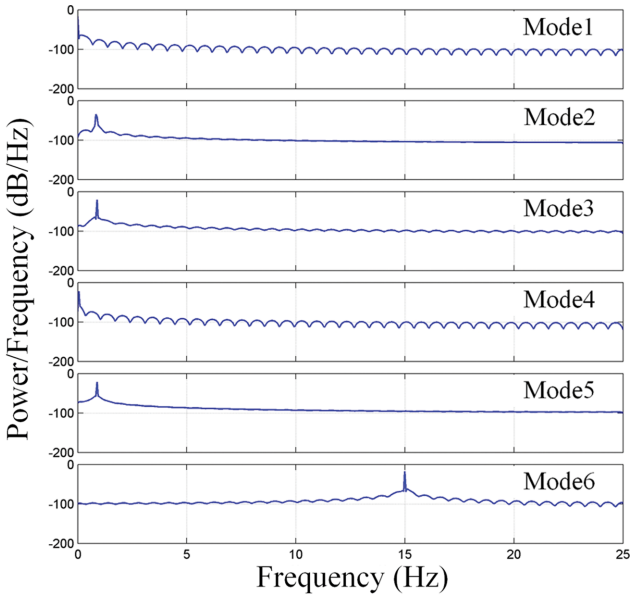


Fig. 18. PSD distribution of modes (1-6).

The second and fifth order modal frequencies are broadly the same, ranging from about 0 to 1 Hz, while the sixth mode frequency is 15 Hz, which is consistent with the blade passage frequency. The velocity signals are subject to decomposition using the DMD method at different rotational speeds. Fig. 19 presents the 2-norms distribution at different rotational speeds and reveals the similar distribution law. Except for the average flow, the peak amplitudes are blade passage frequency and the unstable structure frequency formed by cyclic shear flow.

Due to the difference of calculation method applied, DMD mode exhibits a single frequency. The frequency and spatial distribution of DMD modes are distinct from the POD method, which causes the energy between modes to be different. The order of some modes as obtained by the two decomposition methods is different as well. With regard to periodic flow and quasi-periodic flow, both methods are capable of extracting the large-scale flow structure well. Moreover, there is a high similarity in the extracted flow structures.

4. Discussion

The modal decomposition method provides an effective method to analyze the unsteady turbulent motion and the temporal-spatial correlation characteristics of turbulent. The POD and DMD techniques represent the two most significant methods. As the modal decomposition methods based on global stability, they require only a set of spatiotemporal data to decompose the main frequency (DMD) or main energy content (POD) modes and the spatial characteristics of the corresponding modes without relying on any specific basis functions.

Upon comparison and analysis, there are some differences discovered between POD and DMD in the extraction of spatial coherent structures. POD method is premised on second-order statistical data to perform decomposition. Covariance matrix of spatiotem-

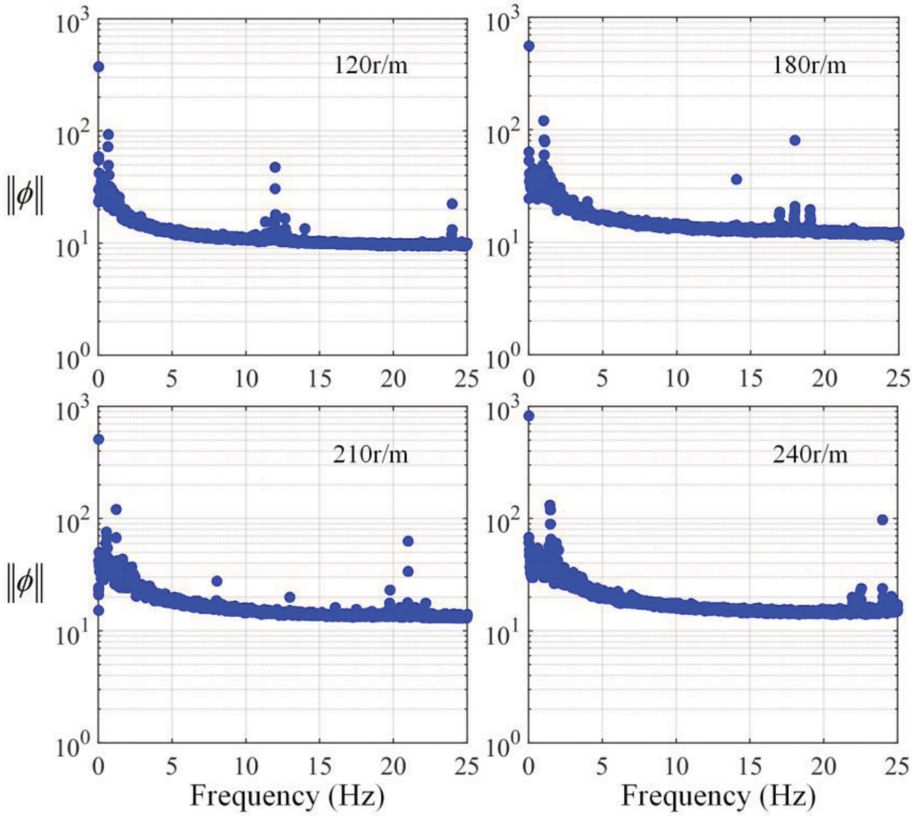


Fig. 19. Amplitude distribution of 2-Norms at different speeds.

poral correlation matrix is applied to obtain the coherent structure of different energy levels. The spatial characteristics of different modes are determined by decomposition based on energy. Dynamic modal decomposition is carried out to extract the dominant coherent structures from a series of transient velocity fields through linear mappings between approximate snapshots. DMD is used to decompose the velocity system orthogonally along the time direction for the purpose of obtaining the modal information at different frequencies.

In consideration of time-frequency, by comparing the distribution of time coefficients, it is found that dynamic mode decomposition is capable of separating and extracting different frequency modes from the velocity system matrix. Each mode contains the distribution of spatial structure at a single frequency. The different modes under POD decomposition are developed by the spatial structure at different frequencies. Not only can dynamic mode decomposition account for the spatial distribution of coherent structures, it also decomposes the modal information of different frequencies with consistent distribution.

Despite the differences between the two methods, there are various correlations between DMD and POD, especially for periodic and quasi-periodic flow. Additionally, the modes show a tendency to be similar and complementary as revealed by the two methods.

The flow structure at a specific frequency can be obtained by phase-resolved velocity field, such as the wake structure. As for stirring process, the POD and DMD decomposition of instantaneous velocity signals is incapable of obtaining the relationship between flow structure and blade phase angle in an accurate way. For the flow structure with accurate phase angle to be obtained, the phase-locked velocity signal can be decomposed using POD method, and the flow structure with different energy can be decoupled [30].

CONCLUSION

An investigation was conducted into the flow structure in a square stirred tank without baffles and with a Rushton impeller by applying PIV technique. The instantaneous flow fields were obtained as a function of various rotations of the impeller (N=120, 150, 180, 210 and 240 rpm), and phase-resolved velocity information was obtained for N=150 rpm. The POD and DMD methods were applied to analyze the flow fields, flow structure and dynamic information of the fluid flow without impeller area. As indicated by the results, the stirring process shows a large span of spatial and temporal scale [15]. Both POD and DMD methods can be effective in obtaining the main flow structure and dynamic information of the periodic flow. The high energy component is reflected in the two flow structures, except for average flow, instability structure formed by cyclic shear flow, the vortex structure induced by the blade passage frequency jet flow. As the speed is on the rise, the stability of the system improves, the low frequency overtones energy of the average flow declines, and the influence is reduced. Due to the structure of the impeller, the two cycles formed by the fluid jet are close to two independent regions. Owing to the different installation position of the impeller and the different restriction conditions on the both sides of the impeller, the evolution structure of the wake vortex shows difference, and the inclination angle of the jet is formed. The square section acts like baffles to cause a change in the direction of the fluid circumferential velocity while enhancing the radial and tangential flow, which is conducive to mixing. As the Reynolds number increases, the periodic flow increases, the random turbulence is in decline, and the flow shows a tendency to the ultimate stable state. As for stirring process, the ultimate stable state will contribute to the increase in energy content of large-scale coherent structure, solidification of flow structure, extension of stirring time, local concentration difference and by-products. Therefore, it is necessary for the optimum operating conditions to be further determined based on the practical conditions of mixing or reactant system. It is hoped to provide a basis for better understanding the flow structure and unsteady flow characteristics.

ACKNOWLEDGEMENTS

This research is supported by the National Natural Science Foundation of China (11572357).

REFERENCES

1. K. V. Sharp and R. J. Adrian, *AIChE J.*, **47**(4), 766 (2001).
2. R. Escudié, D. Bouyer and A. Liné, *AIChE J.*, **50**(1), 75 (2004).
3. H. Unadkat, C. D. Rielly, G. K. Hargrave and Z. K. Nagy, *Chem. Eng. Res. Design*, **8**(7), 573 (2009).
4. A. Delafosse, M. L. Collignon, M. Crine and D. Toye, *Chem. Eng. Sci.*, **66**(8), 1728 (2011).
5. J. L. Lumley, *Stochastic tools in turbulence*, Dover publications, Publication, New York (2007).
6. L. Sirovich, *Quart. Appl. Math.*, **45**, 561 (1987).
7. A. Liné, *Chem. Eng. Res. Des.*, **108**, 13 (2015).
8. P. J. Schmid, *J. Fluid Mech.*, **656**, 5 (2010).
9. P. J. Schmid, *Exp. Fluids*, **50**(4), 1123 (2011).
10. C. W. Rowley, I. Mezić, S. Bagheri, P. Schlatter and D. S. Henningson, *J. Fluid Mech.*, **641**, 115 (2009).
11. S. Roy, J. C. Hua, W. Barnhill, G. H. Gunaratne and J. R. Gord, *Phys. Rev. E*, **91**(1), 013001 (2015).
12. A. Cesura, C. Carlssona, A. Feymarkb, L. Fuchsa and J. Revstedta, *Comput. Fluids*, **101**, 27 (2014).
13. P. J. Schmid, D. Violato and F. Scarano, *Exp. Fluids*, **52**(6), 1567 (2012).
14. Q. Zhang, Y. Liu and S. Wang, *J. Fluids Struct.*, **49**, 53 (2014).
15. A. D. Lamotte, A. Delafosse, S. Calvo and D. Toye, *CES*, **178**, 348 (2018).
16. J. Moreau and A. Line, *AIChE J.*, **52**(7), 2651 (2006).
17. Z. Doulgerakis, M. Yianneskis and A. Ducci, *AIChE J.*, **57**(11), 2941 (2011).
18. J. C. Gabelle, J. Morchaina, D. Anne-Archard, F. Augier and A. Liné, *AIChE J.*, **59**(6), 2251 (2013).
19. A. Liné, J. C. Gabelle, J. Morchaina, D. Anne-Archard and F. Augier, *Chem. Eng. Res. Design*, **91**(11), 2073 (2013).
20. J.-C. Gabelle, J. Morchain and A. Liné, *Chem. Eng. Technol.*, **40**(5), 927 (2017).
21. C. H. Sohn, M. G. Ju and B. H. L. Gowda, *J. Mech. Sci. Technol.*, **24**(4), 951 (2010).
22. C. Wang, Y. Xu, Y. Wu and Z. An, *Can. J. Chem. Eng.*, **96**(11), 788 (2018).
23. H. A. Jakobsen, *Single phase flow*, Springer, Berlin, Heidelberg, 3

(2008).
24. R. J. Adrian and J. Westerweel, *Particle image velocimetry*, Cambridge University Press, Publication, Cambridge (2010).
25. H. Choi, J. Lee and H. Park, *Fluids*, **31**(1), 015102 (2019).
26. M. Raffel, C. E. Willert, S. T. Wereley and J. Kompenhans, *Particle image velocimetry*, A practical guide Springer-Verlag, Publication, Berlin (1998).
27. J. L. Lumley, *Stochastic tools in turbulence*, Dover Publications, N.Y., USA (2007).
28. A. Ruhe, *Linear Algebra Appl.*, **58**, 391 (1984).
29. W. Y. C. Chen and J. D. Louck, *Linear Algebra Appl.*, **232**, 261 (1996).
30. H. K. Chung, M. J. H. Simmons and M. Barigou, *Ind. Eng. Chem. Res.*, **48**, 1008 (2009).
31. J. Zhou, R. J. Adrian and S. Balachandar, *J. Fluid Mech.*, **387**, 353 (1999).
32. M. Eng and A. Rasmuson, *Chem. Eng. J.*, **259**, 900 (2015).
33. Z. Doulgerakis, M. Yianneskis and A. Ducci, *AIChE J.*, **57**(11), 2941 (2011).